


Plasmonic HEMT Terahertz Transmitter based on the Dyakonov-Shur Instability: Performance Analysis and Impact of Nonideal Boundaries

Mona Nafari,^{1,*}† Gregory R. Aizin,² and Josep M. Jornet¹

¹*Department of Electrical Engineering, University at Buffalo, The State University of New York (SUNY), New York, USA*

²*Kingsborough College, The City University of New York (CUNY), New York, USA*

 (Received 1 August 2018; revised manuscript received 29 September 2018; published 11 December 2018)

The performance of an on-chip Terahertz (THz) source based on the Dyakonov-Shur (DS) instability is analytically and numerically investigated. The impact of nonideal termination impedances at the source and the drain of a III-V semiconductor-based HEMT-like plasmonic cavity is first studied in the linear approximation of the hydrodynamic model. Then, a multiphysics simulation platform that self-consistently solves the full hydrodynamic model and Maxwell's equations is developed and utilized to numerically investigate the effects of the finite termination impedances on the DS instability, the generated plasmonic current, and the radiated THz electromagnetic signals in the steady state. The results show that nonideal boundary conditions at the cavity terminations can drastically impact the DS instability and reduce the generated and radiated THz em signals.

DOI: [10.1103/PhysRevApplied.10.064025](https://doi.org/10.1103/PhysRevApplied.10.064025)

I. INTRODUCTION

Over the last decades, wireless data traffic has drastically increased due to a change in the way today's society creates, shares, and consumes information. The massive growth in the total number of mobile connected devices (over 8.0 billion in 2016) has been accompanied by an increasing demand for higher wireless data rates (approaching the 1 Terabit-per-second mark) [1]. To satisfy such a demand, sophisticated communication schemes (e.g., massive multiple-input multiple-output) as well as new spectral bands are needed. In this context, Terahertz (THz)-band (10 THz) communication is envisioned as a key wireless technology for future communication networks [2,3].

For many years, the lack of compact high-power signal sources and high-sensitivity detectors able to work at RT has hampered the use of the THz band in practical communication systems. To date, different technologies are being considered to close the so-called THz gap. In an *electronic approach*, the limits of standard silicon CMOS technology [4], silicon-germanium bipolar junction CMOS transistor technology [5], and III-V semiconductor HEMT, metamorphic HEMT, and HBT technologies [6] are being pushed to reach the 1 THz mark. These systems commonly rely on frequency-multiplying chains to up-convert a multi-GHz local oscillator to THz frequencies. Power loss due to the generation of undesired

harmonics and limited gain of these devices when approaching true THz frequencies hamper the energy efficiency and limit the feasibility of this approach for higher frequencies. In an *optics or optoelectronic approach*, besides photoconductive antennas [7] and optical downconversion systems [8], which would require separate on-chip optical sources, quantum cascade lasers (QCLs) [9] are potential candidates for high-power THz-band signal generation. These lasers can yield THz emission across a broad spectrum, offering output in the range of tens of milliwatts at cryogenic temperatures. However, they suffer from poor performance at RT.

In parallel to these approaches, a promising alternative to realizing THz communications is to leverage the properties of plasmonic materials to develop compact on-chip THz sources. Among others, a III-V semiconductor-based HEMT-like structure, with a two-dimensional (2D) electron gas (2DEG) channel that is formed at a high-quality heterointerface, can be utilized to electrically excite 2D plasmons at THz frequencies. In particular, when a dc current is passed through the HEMT channel, spontaneously excited plasmons drift with the 2D electron fluid. The electron drift causes the Doppler shift in the plasmon dispersion. Plasmon reflection from the channel boundaries reverses the Doppler shift and may result in the amplification of the plasma wave amplitude. Dyakonov and Shur [10] have shown that if the plasmon reflection conditions at the opposite ends of the channel (the drain and the source boundaries) are asymmetric, the instability may be developed when the amplitude of the plasma wave increases

*monanafa@buffalo.edu

†<http://ubnano.tech>

exponentially, provided that the plasma wave gain exceeds the damping losses—the Dyakonov-Shur (DS) instability. In the nonlinear regime, the plasmonic system is stabilized, and in the steady state, the power provided by the external dc circuit is balanced by the combined losses due to scattering and em radiation at the plasmon frequency in the THz range.

The DS instability has been studied experimentally in a number of publications [11–15]. For typical HEMT parameters, the frequency of the unstable plasma modes lies in the THz range, and significant effort has focused on implementing a THz transmitter based on this effect [15]. These efforts have been largely unsuccessful because the em power radiated into free space has proved to be too weak for practical use [14,15]. One of the main reasons behind this problem is the complexity introduced when creating the asymmetric boundary conditions in the HEMT.

The effect of the nonideal boundary conditions on the DS instability was also considered in a number of publications [16–19]. Most of the studies [16,17] have been concerned with the effect of the interface between the 2D electron channel and three-dimensional (3D) metal drain and source contacts on the electron density and electric potential in the 2D channel near the contact. This effect is important for calculations of the plasmon spectrum in the 2D electron channel of finite length (plasmonic cavity). However, the interfaces at the opposite sides of the 2D electron channel are technologically identical and do not contribute to the asymmetry necessary for the DS instability. The asymmetry stems from the different ac electric links (displacement currents) between the 2D channel and surrounding electrodes at the opposite edges of the channel. These links can be described in terms of the complex impedances. In the original paper by Dyakonov and Shur [10], it was assumed that the impedance between the source and the gate approaches zero ohm, and the impedance between the drain and the gate tends to infinity, something which practically cannot be realized. Similarly, in a wireless communication system, the need to attach the source to a modulator or ultimately an antenna will further modify such an impedance.

The effect of the finite gate-source and gate-drain impedances on the increment of the DS instability was first considered in the early paper by Cheremisin and Samsonidze [18]. These authors derived a general expression for the instability increment valid at arbitrary values of the terminating impedances and demonstrated that the instability is retained as long as the value of the gate-drain impedance exceeds the value of the gate-source one. Also, the effect of the finite capacitive impedances between the source and drain contacts and the gate on the performance of the plasmonic THz detector based on the FET was considered in the very recent paper by Svintsov [19].

In this paper, we analytically and numerically investigate the HEMT-like on-chip THz transmitter based on

the DS instability and impact of the nonideal boundary conditions at the source and drain contacts on its performance. First, using the transmission line analogy, we develop a new analytical model for the DS instability in the 2D electron layer with finite impedances at the source and drain (Sec. II). We derive an expression for the complex plasma frequency and demonstrate how the DS instability frequency and increment depend on the finite terminating impedances and other parameters of the HEMT structure. Then, we develop a comprehensive finite-difference time-domain numerical solver that consistently solves the hydrodynamic model equations and Maxwell’s equations (Sec. III). By utilizing this tool, we numerically validate the developed analytical model and study the impact of nonideal boundary conditions at the source and drain of the device on the generated and radiated em fields in the steady state. Our results show that nonideal boundary conditions can not only reduce the generated power by the THz source, but can effectively prevent the instability from arising. We quantitatively show that, provided that the source impedance is much lower than the HEMT intrinsic impedance and both are much lower than the drain impedance, the DS instability will develop and the HEMT structure in steady state becomes a THz transmitter. These results emphasize the need to engineer the drain and source impedances, in addition to the drift velocity and the electron relaxation time, to enable DS-instability-based on-chip THz sources.

II. ANALYTICAL MODEL

A. Basic equations

Collective plasma excitations in the 2DEG in the HEMT conduction channel with a dc can be described by the hydrodynamic model [20]. In this model, the 2DEG is characterized by the local electron density $n(\mathbf{r}, t)$ and velocity $v(\mathbf{r}, t)$ obeying the Euler and continuity equations. For a plasmon propagating in the x direction in the 2DEG layer positioned in the plane $z = 0$, these equations are

$$\frac{\partial v}{\partial t} + v \frac{\partial v}{\partial x} = -\frac{e}{m_e^*} E_x - \frac{1}{nm_e^*} \frac{\partial P}{\partial x} - \frac{v}{\tau}, \quad (1)$$

$$\frac{\partial n}{\partial t} + \frac{\partial (nv)}{\partial x} = 0. \quad (2)$$

Here, P stands for the local pressure in the 2D electron fluid, E_x is the x component of the self-consistent electric field in the channel, and $-e$ and m_e^* are the electron charge and effective mass, respectively. A phenomenological damping term included in the Euler equation in Eq. (1) accounts for the collisional damping of the plasmon with the characteristic relaxation time τ . At typical electron densities, the 2DEG in the HEMT channel remains degenerate in the broad range of temperatures up to RT. In the

degenerate limit, the 2D electron pressure P in Eq. (1) depends on the electron density n as

$$P = \frac{\pi \hbar^2 n^2}{2m_e^*}. \quad (3)$$

Equations (1) and (2) should be solved together with Maxwell's equations for the plasmon em field to obtain a self-consistent solution. This will be numerically done in Sec. III. In this section, in order to provide an intuitive analytical model, we limit our consideration of the plasma oscillations to the linear analysis sufficient to determine conditions necessary for triggering the plasma instability and growth of the amplitude of the plasma wave. In this case, the em field can be found in the quasi-static approximation by using the Poisson equation for the self-consistent electric potential $\varphi(\mathbf{r}, t)$ of the plasma wave

$$\nabla_{x,z}^2(\varphi) = \frac{en}{\epsilon_0 \epsilon} \delta(z), \quad (4)$$

$$E_x = -\frac{\partial \varphi(x, z=0)}{\partial x}, \quad (5)$$

where ϵ is the relative permittivity of the surrounding medium.

We linearize Eqs. (1)–(3) with respect to the small fluctuations of the electron density $\delta n(x, t)$ and average velocity $\delta v(x, t)$ assuming that $n = n_0 + \delta n$, $v = v_0 + \delta v$, where n_0 is the equilibrium electron density and v_0 is the constant electron drift velocity due to dc source-drain bias. For one Fourier Harmonic $\delta n, \delta v, \varphi \propto e^{-ikx+i\omega t}$ we obtain the system of linear algebraic equations for the charge density $\rho = -e\delta n$ and electric current density $j = -e(n_0\delta v + v_0\delta n)$ in the plasma wave, which should be solved together with the Poisson equation connecting ρ and ϕ . Electric potential is connected with the fluctuation of electron density by Eq. (4). When the ideal metal gate is separated by a distance d from the channel, Eq. (4) yields the following relation between φ and ρ [21]:

$$\varphi = \frac{\rho}{|k|\epsilon\epsilon_0(1 + \coth|k|d)}. \quad (6)$$

A nontrivial solution for j and φ exists only if

$$(\omega - kv_0) \left(\omega - kv_0 - \frac{i}{\tau} \right) = \frac{e^2 n_0 |k|}{m_e^* \epsilon \epsilon_0 (1 + \coth|k|d)} + \frac{1}{2} k^2 v_{v_F}^2, \quad (7)$$

where v_F is the Fermi velocity in the degenerate 2DEG. The last equation is the dispersion equation for the drifting plasmon in the gated 2D electron channel. It can be

further simplified if we assume that the collisional damping is small $\omega\tau \gg 1$ and the gate-to-channel separation d is much smaller than the plasmon wavelength $kd \ll 1$. As shown below, the typical plasmon wavelength is of the order of the source-drain distance so the last assumption is justified. With these assumptions, the drifting plasmon dispersion law takes the simple form

$$\omega = (v_0 \pm v_p)k + \frac{i}{2\tau}, \quad (8)$$

where sign \pm corresponds to the Doppler-shifted acoustic plasmons propagating in the opposite directions, and

$$v_p = \sqrt{\frac{e^2 n_0 d}{\epsilon_0 \epsilon m_e^*} + \frac{v_F^2}{2}}, \quad (9)$$

is the plasmon velocity in the absence of the drift. This last result differs from the well-known expression for the velocity of the gated plasmon [21] by the correction $v_F^2/2$. This correction results from the inclusion of the pressure term into the Euler equation.

The general expressions for the voltage $V(x, t) = \varphi(x, z=0, t)$ and the current $I(x, t) = j(x, t)W$ in the plasma wave of frequency ω propagating in the gated channel of width W are

$$V(x, t) = C_1 e^{-ik_+x+i\omega t} + C_2 e^{-ik_-x+i\omega t}, \quad (10)$$

$$I(x, t) = \frac{C_1}{Z_0} \left(1 + \frac{v_0}{v_p} \right) e^{-ik_+x+i\omega t} - \frac{C_2}{Z_0} \left(1 - \frac{v_0}{v_p} \right) e^{-ik_-x+i\omega t}, \quad (11)$$

where $k_{\pm} = (\omega - \frac{i}{2\tau})/(v_0 \pm v_p)$ are the complex wave numbers of the plasma wave propagating in the direction of the drift (+) and in the opposite direction (-) and $Z_0 = d/\epsilon\epsilon_0 v_p W$. Constants C_1 and C_2 are determined by the boundary conditions.

B. The Dyakonov-Shur instability

The physical mechanism of the DS instability described in the Introduction is based on the asymmetric reflection of the drifting plasma waves at the opposite ends of the plasmonic cavity formed in the gated region of the 2D conduction channel in the HEMT. The very general description of this reflection can be obtained by introducing the terminating complex impedances between the 2D channel and the gate at the ends of the plasmonic cavity. This approach is based on the analogy between the plasma wave propagation in the gated 2D channel and an ac signal propagation in the transmission line [22].

We assume that an ac link between the 2D channel and the gate is purely reactive and choose the terminating impedances as iZ_S and iZ_D where subscripts “S” and “D” refer to the source and drain sides of the plasmonic cavity and Z_S, Z_D have real values. In this approximation, we neglect the resistive part of the terminating impedances responsible for the leakage of the plasma wave from the cavity to the source and drain contacts with the loss of the real power. Now the boundary conditions for the plasma waves in the plasmonic cavity of length L with terminating impedances iZ_S at $x = 0$ and iZ_D at $x = L$ are

$$V(0, t) = -iZ_S I(0, t), \quad (12)$$

$$V(L, t) = iZ_D I(L, t). \quad (13)$$

These conditions connect the local values of the plasmonic current and the electric potential at the source and the drain edges of the plasmonic cavity. The opposite signs in the right-hand sides of these two equations are due to the reversed directions of the currents at the opposite ends of an isolated cavity. The boundary conditions (12) and (13) are valid as long as the gate-channel separation is small compared with the plasma wavelength, $kd \ll 1$. In this limit, the TEM-like plasma wave propagates in the channel and can be described in the approximation of the local gate-channel capacitance when the current in the gate mimics the channel current, but with the opposite sign [23]. Equations (10)–(13) solved together determine the dispersion equation of the plasma modes in the cavity as

$$e^{2(\omega - \frac{v_0}{2\tau})L/v_p(1 - v_0^2/v_p^2)} = \frac{[1 - (iZ_D/Z_0)(1 + v_0/v_p)][1 - (iZ_S/Z_0)(1 - v_0/v_p)]}{[1 + (iZ_D/Z_0)(1 - v_0/v_p)][1 + (iZ_S/Z_0)(1 + v_0/v_p)]}. \quad (14)$$

The last equation yields a complex plasma frequency $\omega = \omega' + i\omega''$. In the practically important limit $v_0/v_p \ll 1$, we obtain

$$\omega' = \frac{v_p}{L}(\pi n - \varphi_S - \varphi_D), \quad n = 1, 2, \dots, \quad (15)$$

$$\omega'' = -\left[\frac{v_0}{L}(\cos^2 \varphi_S - \cos^2 \varphi_D) - \frac{1}{2\tau} \right], \quad (16)$$

where

$$\tan \varphi_{D,S} = \frac{|Z_{D,S}|}{Z_0}. \quad (17)$$

It follows from Eqs. (15)–(17) that both the plasma frequency ω' and the plasma wave increment/decrement ω'' strongly depend on the values of the terminating impedances Z_D and Z_S . The frequency shift depends on

the ratio $|Z_{D,S}|/Z_0$, and the plasma frequency may significantly deviate from its ideal values at $Z_S = 0$ and $Z_D = \infty$. The magnitude of ω'' depends on the relative values of $|Z_D|$ and $|Z_S|$, but also strongly depends on the $|Z_{D,S}|/Z_0$ ratio. The impedance Z_0 can be interpreted as the characteristic impedance of the plasmonic transmission line [22]. Inequality $\omega'' < 0$ is the condition of the DS instability in the plasma wave. It follows from Eqs. (15) and (16) that the DS instability occurs only if $|Z_D| > |Z_S|$ [18] at drift velocities v_0 larger than some threshold value increasing at short relaxation times. The proper tuning of the terminating impedances with respect to Z_0 may increase the instability increment. The expression for the instability increment with boundary conditions (12), (13) was first derived in Ref. [18] at arbitrary values of v_0/v_p . This expression can be reduced to Eq. (16) at $v_0/v_p \ll 1$. The ideal case corresponding to $Z_S = 0, Z_D \rightarrow \infty$, was considered in the original paper by Dyakonov and Shur [10]. In this limit, Eqs. (15)–(17) reproduce the results found in this paper at $v_0 \ll v_p$.

III. NUMERICAL ANALYSIS OF THE DS INSTABILITY IN SEMICONDUCTOR HEMTS

The analytical solutions are obtained within the first-order perturbation theory, and thus are only valid when the fluctuations are small. Less restrictive numerical simulations, which can capture the impact of the geometry, additional plasma damping due to finite electron momentum relaxation time, and the finite values of the terminating impedances are needed for comprehensive study of the HEMT THz device performance. The growing plasma oscillations are stabilized due to the nonlinear processes [24,25], and in the final steady state, the plasmonic power gain is balanced by the emitted em radiation and scattering losses. In this case, the plasma wave amplitude is not small, and the perturbation theory is not applicable. Also, the full system of Maxwell’s equations should be used to describe the em radiation in the steady state. Numerical simulations of the DS instability have been reported in Refs. [25,26]. The authors of Ref. [26] consider the DS instability in the ungated transistor structure, ignoring effects of the gate and terminating impedances on the instability. In Ref. [25], numerical solution of the hydrodynamic equations together with the Poisson equation in the gated transistor structure is presented. In this approach, the effect of the em radiation is not directly included into the numerical formalism and the estimates of the radiated em power are performed indirectly based on the analysis of the static current-voltage characteristics. Below we present our analysis of the performance of the HEMT THz emitter based on the numerical solution of the hydrodynamic equations together with the full system of Maxwell’s equations. We analyze the final steady state of the HEMT THz emitter including the effects of the plasmon collisional

damping and finite terminating impedances, determine the em radiation pattern, and directly calculate the emitted em power.

A. Multiphysics simulation platform

To numerically analyze plasma waves in the on-chip THz source, the hydrodynamic model equations describing the evolution of the electron density n , velocity v , and current density $j = -env$ in the 2DEG layer and Maxwell's equations describing the evolution of the electric E and magnetic H fields have to be self-consistently solved together. Since existing commercial tools cannot simultaneously solve both hydrodynamic and Maxwell's equations in the time domain, we have developed a finite-difference time-domain (FDTD) multiphysics simulation platform. In the developed platform, the electron dynamics in the 2DEG layer is described by solving the hydrodynamic model equations Eqs. (1) and (2). To compute E_x in Eq. (1), we now solve Maxwell's equations

$$\nabla \times \mathbf{E} = -\mu_0 \frac{\partial \mathbf{H}}{\partial t}, \quad (18)$$

$$\nabla \times \mathbf{H} = \mathbf{J} + \varepsilon \varepsilon_0 \frac{\partial \mathbf{E}}{\partial t}. \quad (19)$$

Here, $\mathbf{E} = E_x \hat{x} + E_y \hat{y}$ and $\mathbf{H} = H_z \hat{z}$ refer to the electric and magnetic fields' vectors, respectively, the current density vector $\mathbf{J} = J_x \hat{x}$ is related to the surface current density j in the 2DEG as $J_x = j/t_{2\text{DEG}}$ where $t_{2\text{DEG}}$ is the thickness of the 2DEG layer.

Stabilizing a fully explicit discretization of the governing equations for such a highly nonlinear system of differential equations as the hydrodynamic model equations is a critical task. A slight change in the discretization strategy may cause computational instability and direct application of common discretization methods does not lead to the physically correct results. The order in how the various quantities (n , v , j , \mathbf{E} , \mathbf{H}) are updated is also of crucial importance. In our analysis, we follow the methodology introduced in [27] to simulate the 2DEG as a one-dimensional (1D) system and utilize the *up-wind* approach to stabilize the discretization of the system. Then, we use a homogeneous and uniform mesh to generalize to two dimensions for the em solver [28–30]. In the Appendix, we provide the derivation of the finite-element discretization of the governing equations and the conditions for the system to be numerically stable.

In Fig. 1, we illustrate the reference structure simulated in our analysis. It consists of a HEMT-like structure, built with a III-V semiconductor material with permittivity ε and metallic gate and source and drain contacts with conductivity σ . The 2DEG layer is characterized by the electron density n , velocity v , effective electron mass m_e^* ,

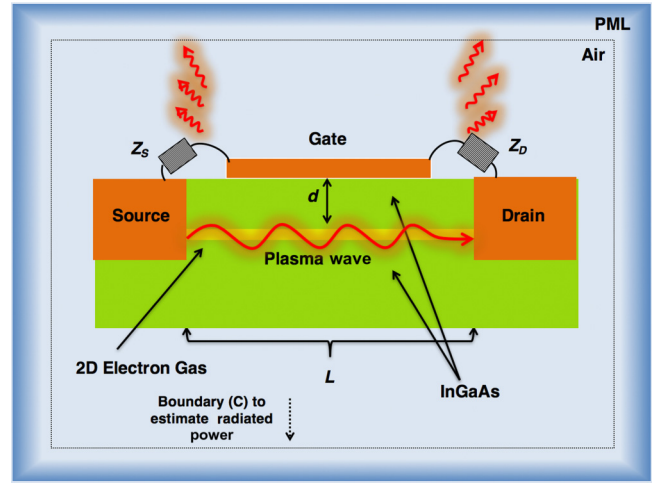


FIG. 1. Schematic of the HEMT structure used for numerical simulations.

and electron momentum relaxation time τ . It is positioned at a distance d under the gate, and has an effective thickness $t_{2\text{DEG}}$. The impedances between the source and the gate and the gate and the drain are given by Z_S and Z_D , respectively. The HEMT is considered to be in an air-filled box delimited by a Perfectly Matched Layer (PML). The latter is needed to emulate an infinite space when solving Maxwell's equations and prevents artificial reflections at the box boundaries.

B. Numerical results

In this section, we numerically investigate the behavior of the DS plasma instability in the gated (In,Ga)As-based HEMT structure shown in Fig. 1, with 2DEG channel length $L = 110$ nm, gate length $L_g = 100$ nm extended from source to drain with 5 nm separation from ohmic contacts at source and drain. We consider the gate and source and drain contacts to be made of a nearly ideal metal with $\sigma = 10^7$ S/m, channel depth $d = 20$ nm, channel width $W = 100$ μm , 2DEG layer thickness $t_{2\text{DEG}} = 5$ nm, $\varepsilon = 13$, $m_e^* = 0.04m_0$. We initialize the whole channel with equilibrium electron density $n_0 = 2.2 \times 10^{15}$ m^{-2} and constant drift velocity v_0 , and apply initial excitation by doubling the electron density at the channel length of 5 nm next to the drain contact. Then we record the time dependence of the plasmonic ac current in the 2DEG channel. Our numerical algorithm, including the implementation of different boundary conditions, is described in detail in the Appendix.

1. Impact of drift velocity v_0 and relaxation time τ

In this numerical study, we assume the ideal boundary conditions $Z_S = 0$, $Z_D = \infty$ and recorded the time dependence of the plasmonic ac current near the drain contact after initial excitation. It follows from Eq. (16) that under

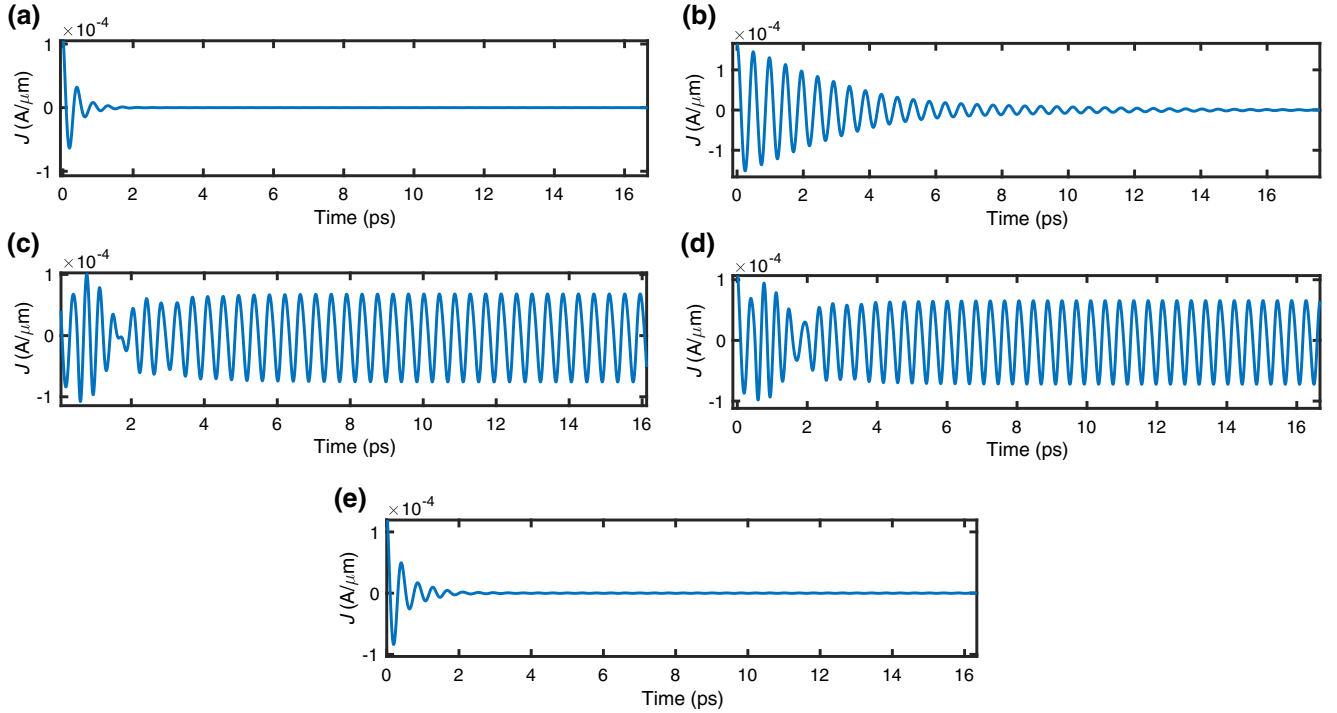


FIG. 2. Plasmonic THz current density J as a function of time at different drift velocities v_0 and electron relaxation times τ . The gate-source impedance $Z_S = 0$, the gate-drain impedance $Z_D = \infty$. (a) $\tau = 0.01$ ps, $v_0 = 4 \times 10^5$ m/s. (b) $\tau = 0.1$ ps, $v_0 = 4 \times 10^5$ m/s. (c) $\tau = 1$ ps, $v_0 = 4 \times 10^5$ m/s. (d) $\tau = 1$ ps, $v_0 = 1 \times 10^5$ m/s. (e) $\tau = 1$ ps, $v_0 = 0.2 \times 10^5$ m/s.

the ideal boundary conditions, the instability occurs when the electron transit time in the HEMT $\tau_{tr} = L/v_0$ is shorter than 2τ [10]. Our numerical results are presented in Fig. 2.

In Figs. 2(a) through 2(c) we assume $v_0 = 4 \times 10^5$ m/s so that the electron transit time $\tau_{tr} = 0.275$ ps, and recorded the current signal at different values of the electron relaxation time. For the values of $\tau = 0.01$ ps and $\tau = 0.1$ ps in Figs. 2(a) and 2(b) respectively, we have $\tau_{tr} > 2\tau$, and the plasmonic current signal decays rapidly after the initial excitation because the power losses due to random electron scattering exceed the power gain due to plasmon reflections from the asymmetric boundaries. In Fig. 2(c), the value of τ is 1ps and $\tau_{tr} < 2\tau$. In this case, the power gain at the plasmon reflections from the asymmetric boundaries starts to exceed the scattering losses, and the DS instability develops. The oscillating THz plasmonic current stabilizes at some finite amplitude with the combined losses due to scattering and em radiation balancing the power gain.

Decreasing electron drift velocity makes the electron transit time longer and the instability eventually disappears. This is shown in Figs. 2(d) and 2(e) where we recorded the time dependence of the current at $\tau = 1$ ps, but $v_0 = 1 \times 10^5$ m/s and $v_0 = 0.2 \times 10^5$ m/s, respectively. In Fig. 2(d) the value of $\tau_{tr} = 1.1$ ps is less than 2τ and the instability still exists. However, with further decrease of v_0 , the DS instability disappears as shown in Fig. 2(e) where $\tau_{tr} = 5.5$ ps.

2. Impact of source and drain impedances

In the HEMT plasmonic cavity formed in the 2D channel between the source and the drain terminal, the DS instability is maximized under the ideal boundary conditions $Z_S = 0$, $Z_D = \infty$. As shown in Eq. (16), the finite source-gate and drain-gate impedances suppress the instability. These impedances are the result of the shunt capacitances always present between the gate and the HEMT source/drain terminals. Calculations show that in the HEMT structures, these capacitances are in the range of tens of femtofarads [11]. At THz frequencies, this corresponds to the impedances lying in the range of tens of ohms. These impedances effectively shunt much larger inductive impedances of the bonding wires and define terminating impedances at the ends of the plasmonic cavity [19]. We numerically studied the impact of the finite gate-source (C_S) and gate-drain (C_D) capacitances on the DS instability in the HEMT structure shown in Fig. 1. In this case, the boundary conditions conforming with Eqs. (12) and (13) are as follows:

$$I(0, t) = -C_S \frac{\partial V(0, t)}{\partial t}, \quad (20)$$

$$I(L, t) = C_D \frac{\partial V(L, t)}{\partial t}, \quad (21)$$

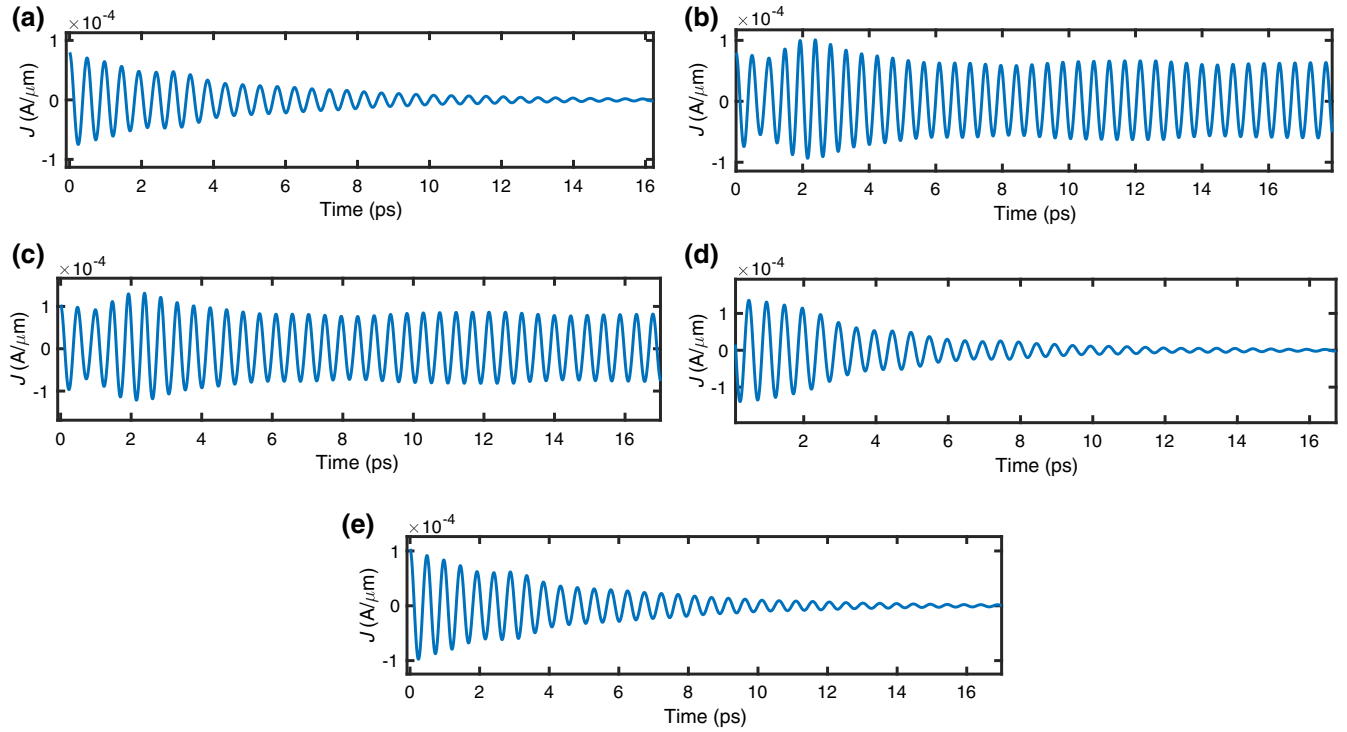


FIG. 3. Plasmonic THz current density J as a function of time at different values of the gate-source (C_S) and the gate-drain (C_D) capacitances. Electron drift velocity $v_0 = 4 \times 10^5$ m/s, electron relaxation time $\tau = 1$ ps. (a) $C_S = 1$ fF, $C_D = 1$ fF. (b) $C_S = 5$ fF, $C_D = 1$ fF. (c) $C_S = 10$ fF, $C_D = 1$ fF. (d) $C_S = 1$ fF, $C_D = 5$ fF. (e) $C_S = 1$ fF, $C_D = 10$ fF.

where $V(x, t)$ is connected to $n(x, t)$ as $V(x, t) = -en(x, t)/C_{GC}$. Here, $C_{GC} = \epsilon\epsilon_0/d$ is the gate-channel capacitance per unit area.

In our numerical simulations, we take $v_0 = 4 \times 10^5$ m/s and $\tau = 1$ ps and record plasmonic current near the drain contact as a function of time. The results are presented in Fig. 3.

In Fig. 3(a), we assume that $C_S = C_D = 1$ fF. In this case, the boundaries become symmetric ($Z_S = Z_D$), the power gain disappears, and the ac plasmonic current rapidly decays due to random scattering of electrons. In Figs. 3(b) and 3(c), asymmetry is introduced by assuming that $C_S = 5$ fF and 10 fF, respectively, and $C_D = 1$ fF so that $Z_D > Z_S$. The power gain due to plasmon reflections from the asymmetric boundaries exceeds the damping losses, and the DS instability develops with finite plasmonic current in the final steady state. If the value of C_S is kept constant, and asymmetry is introduced by increasing the value of C_D so that $Z_D < Z_S$, the current continues to decay as predicted by Eq. (16). This is shown in Figs. 3(d) and 3(e) where $C_S = 1$ fF and $C_D = 5$ fF and 10 fF, respectively.

Rigorous numerical solution of the nonlinear hydrodynamic equations together with the full system of Maxwell's equations is in good qualitative agreement with the results of the linear perturbation analysis of the hydrodynamic equations within the quasi-static model

of the em field presented in Sec. II. However, the full numerical solution goes beyond the linear response and allows analysis of the final steady state of the radiating HEMT system including the structure of the radiated THz em field. This analysis is presented in the next section.

C. Generated electromagnetic fields

In this section, we examine the performance of a HEMT-like structure as a THz em source based on the DS instability by analyzing the properties of the generated fields and the impact of the source and drain impedances on the radiated power.

In Figs. 4(a) and 4(b), the electric field vector components E_x and E_y , respectively, are plotted for the radiating HEMT in the steady state with $\tau = 1$ ps, $v_0 = 4 \times 10^5$ m/s and ideal boundary conditions corresponding to Fig. 2(c). The plots show that the plasma wave in the 2DEG channel generates an em wave in the space between the gate and 2DEG channel, which leaks through the gaps between the source/drain contacts and the gate and eventually propagates over the entire simulation region.

The em power P radiated by the THz source at any given frequency can be calculated by integrating the normal component of the Poynting vector over a continuous

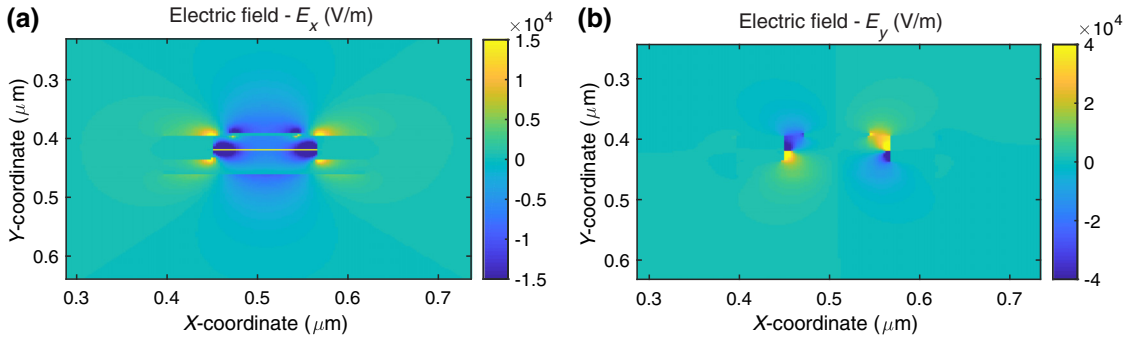


FIG. 4. Electric fields resulting from the DS instability corresponding to Fig. 2(c) (ideal boundary conditions, $\tau = 1$ ps, $v_0 = 4 \times 10^5$ m/s).

boundary that encircles the device as:

$$P = \frac{1}{2} \int_C \text{Re} \left\{ \tilde{\mathbf{E}} \times \tilde{\mathbf{H}}^* \right\} \cdot \mathbf{n} dl, \quad (22)$$

where \mathbf{n} is the unit vector normal to the boundary and $\tilde{\mathbf{E}}$ and $\tilde{\mathbf{H}}$ are complex Fourier transforms of the electric and magnetic field vectors in the time domain at the integration boundary C shown in Fig. 1. In our analysis, we disregard the transient time until the generated currents and fields become stable (approximately the first 2 ps in Figs. 2 and 3).

In Fig. 5, we show the radiated em power spectrum for both ideal and nonideal ($C_S = 10$ fF, $C_D = 1$ fF) boundary conditions at $\tau = 1$ ps and $v_0 = 4 \times 10^5$ m/s. Resonant peaks in the power spectrum occur at the frequencies of plasmons confined in the HEMT cavity with the largest peak at the fundamental frequency of 2.27 THz

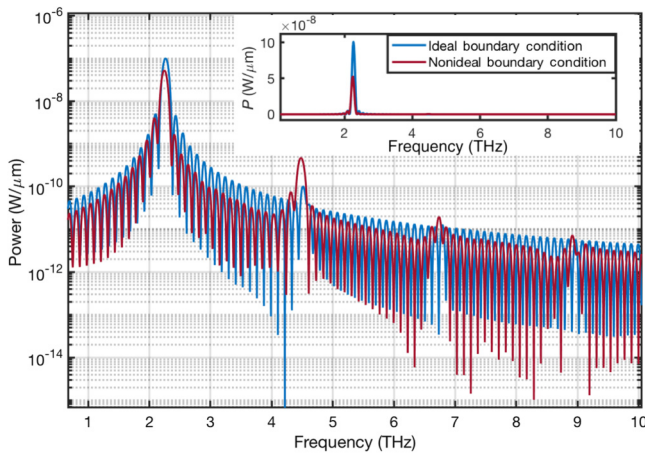


FIG. 5. The radiated em power spectrum for ideal boundary conditions (blue) and nonideal boundary conditions ($C_S = 10$ fF, $C_D = 1$ fF), $\tau = 1$ ps, $v_0 = 4 \times 10^5$ m/s. Inset: the same power spectrum in linear scale, showing the power loss due to nonideal boundary conditions.

and much weaker peaks at higher harmonics. The value of the fundamental plasma frequency estimated from the power spectrum is about 10% larger than the one predicted by the theoretical model in Eq. (14), indicating the difference between a simple theoretical model and more accurate numerical simulation and accounting for the complicated spatial distribution of the em fields in the finite semiconductor structure, see Fig. 4.

At the fundamental frequency, the radiated em power per unit channel width shown in Fig. 5 is about 9×10^{-8} W/ μm under the ideal boundary conditions. In this case, the total radiated power from the device can be estimated as 9×10^{-8} W/ μm \times $100 \mu\text{m} = 9 \mu\text{W}$. The nonideal boundary conditions decrease the instability increment in Eq. (16) and result in the decreased radiated em power. This is shown in the inset in Fig. 5, where the radiated power spectrum is plotted in the linear scale making this difference more clear. When the nonideal boundary conditions are used, the reduction in the radiated power at the fundamental frequency is about 4.2×10^{-8} W/ μm or 46.7%.

IV. CONCLUDING REMARKS

In this paper, we have analytically and numerically investigated the performance of an on-chip HEMT THz transmitter based on the DS instability. We found conditions of instability and its dependence on the various parameters in the realistic finite size HEMT semiconductor structures with metal source, drain, and gate contacts. We also numerically analyzed the HEMT transmitter performance in a steady radiating state and found the em field distribution and the radiated power in different regimes.

Our study shows that finite nonideal drain-gate and source-gate impedances can reduce the strength and even entirely suppress the DS instability when the difference between their values and the ideal ones increases. Similarly, the radiated em power also decreases under nonideal boundary conditions. These results highlight the need to precisely engineer the source and drain

impedances in order to enable the DS instability-based on-chip THz source and are important for its experimental realization.

The developed numerical multiphysics simulation platform allows for self-consistent solution of the hydrodynamic model equations and Maxwell's equations in an air-enclosed HEMT-type structure and can be easily extended to simulate different electronic, plasmonic, and em devices and structures.

ACKNOWLEDGMENTS

This work was partially supported by the Air Force Office of Scientific Research (AFOSR) under Grant no. FA9550-16-1-0188. M.N. thanks Dr. Andreas Aste from University of Basel, Switzerland for useful discussions on discretization methods.

APPENDIX: FINITE-DIFFERENCE TIME-DOMAIN MULTIPHYSICS SIMULATION PLATFORM

The numerical results presented in the paper have been obtained by means of a home-built Finite-Difference Time-Domain (FDTD) platform that consistently solves the hydrodynamic model (HDM) equations and Maxwell's equations. In this section, we describe the implementation of the platform, including the discretization of the scenario under analysis as well as the discretization of the governing equations.

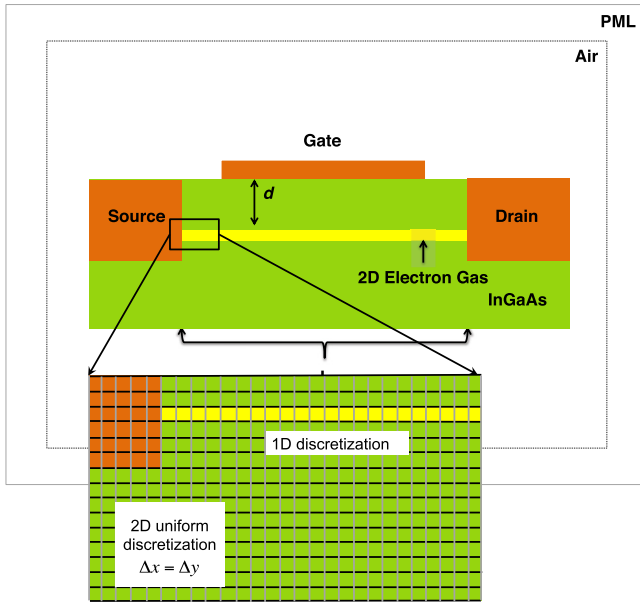


FIG. 6. Schematic of the reference structure and its discretized (meshed) equivalent.

1. Discretization of the Scenario

The first step involves the discretization of the device under analysis. In Fig. 6, we illustrate the reference structure and its meshed equivalent. It consists of a HEMT-like structure, built with a III-V semiconductor material with permittivity ϵ and metallic gate and source and drain contacts with conductivity σ . The 2DEG layer is characterized by the electron density n , velocity v , effective electron mass m_e^* , and electron momentum relaxation time τ . It is positioned at a distance d under the gate, and has a thickness t_{2DEG} . The HEMT is considered to be in an air-filled box delimited by a PML. The latter is needed to emulate an infinite space when solving Maxwell's equations and prevents artificial reflections at the box boundaries [29].

The mesh size along the 2DEG layer is determined by the Debye length criteria inside the semiconductor. To ensure numerical stability, $\Delta t < \Delta x/c$, where c is the speed of light. In our scenario, we consider $\Delta x = 5$ nm and $\Delta t = 10^{-17}$ s. In addition, we define $\Delta y = \Delta x$, and thus, the thickness of the 2DEG is effectively set to $t_{2DEG} = 5$ nm.

2. Discretization of the hydrodynamic model equations in the 2DEG channel

The second step involves the discretization of the HDM equations, which, for convenience, we rewrite as follows:

$$\frac{\partial n}{\partial t} + \frac{\partial \hat{j}}{\partial x} = 0, \quad (\text{A1})$$

$$\begin{aligned} \frac{\partial \hat{j}}{\partial t} + v \frac{\partial \hat{j}}{\partial x} + \hat{j} \frac{\partial v}{\partial t} = & -\frac{ne}{m_e^*} E_x \\ & - n \frac{\pi \hbar^2}{m_e^{*2}} \frac{\exp(E_F/kT)}{\exp(E_F/kT) - 1} \frac{\partial n}{\partial x} - \frac{\hat{j}}{\tau}, \end{aligned} \quad (\text{A2})$$

where $\hat{j} = nv$ is the particle current density in the HEMT channel, E_x is the electric field along the channel, $E_F = \pi \hbar^2 n / m_e^*$ is the 2D gas Fermi energy, T is the system temperature, k is the Boltzmann constant, and τ is the plasmon relaxation time.

We follow the methodology introduced in [27] to discretize and solve the HDM equations in the $N = L/\Delta x$ cells C_i corresponding to the 2DEG (Fig. 6). Scalar quantities such as the electron density n are located at the center of the cells (sub-index i), whereas vectorial quantities such as the current density \hat{j} and v are located at the boundaries of the cells (subindexes $i \pm 1/2$, see Fig. 7).

First, the values of n_i and $\hat{j}_{i+1/2}$ are initialized to n_0 and j_0 , respectively, where n_0 is the equilibrium electron density and v_0 is the constant electron drift velocity due to dc source-drain bias. Then, the value of n_i at the next

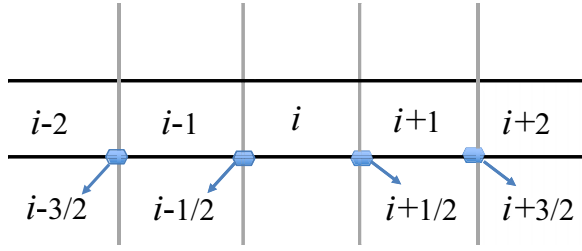


FIG. 7. Location of boundary and center cells for vectorial and scalar quantities, respectively.

time instant is computed from the discretized continuity equation (Eq. (A1)) as follows:

$$\frac{n_i^{t+1} - n_i^t}{\Delta t} = -\frac{\hat{j}_{i+1/2}^t - \hat{j}_{i-1/2}^t}{\Delta x}, \quad (\text{A3})$$

$$n_i^{t+1} = n_i^t - \frac{\Delta t}{\Delta x} (\hat{j}_{i+1/2}^t - \hat{j}_{i-1/2}^t). \quad (\text{A4})$$

Next, we compute the value of the electron density $n_{i\pm 1/2}$ at the boundaries of the cells by following the upwind approach, which is defined as follows:

$$n_{i+1/2}^t = \begin{cases} \frac{3}{2}n_i^t - \frac{1}{2}n_{i-1}^t & \text{if } j_{i+1/2}^t > 0, \\ \frac{3}{2}n_{i+1}^t - \frac{1}{2}n_{i+2}^t & \text{if } j_{i+1/2}^t < 0, \end{cases} \quad (\text{A5})$$

i.e., the electron density is extrapolated from neighboring points in the direction of the electron flow. The upwind extrapolation of the electron density, which is given by the weighting factors $3/2$ and $-1/2$, is improving the accuracy of the scheme compared to the usual upwind choice $n_{i\pm 1/2} = n_i$, where the neighboring value in the upwind direction is used.

We can now compute the electron velocity as

$$v_{i+1/2}^t = \frac{\hat{j}_{i+1/2}^t}{n_{i+1/2}^t}. \quad (\text{A6})$$

At this point, we can discretize the impulse balance (Eq. (A2)), mostly by means of central differences. The stability of the scheme is improved if the current density is first updated by [27]:

$$\begin{aligned} \frac{\hat{j}_{i+1/2}^{t+1} - \hat{j}_{i+1/2}^t}{\Delta t} &= -\frac{e}{m_e^*} n_{i+1/2}^t E_{i+1/2}^t \\ &\quad - n \frac{\pi \hbar^2}{m_e^{*2}} \frac{\exp(E_F/kT)}{\exp(E_F/kT) - 1} \frac{(n_{i+1}^t - n_i^t)}{\Delta x} \\ &\quad - \frac{\hat{j}_{i+1/2}^t}{\tau} - (\text{conv})_{i+1/2}^t, \end{aligned} \quad (\text{A7})$$

and then $\hat{j}_{i+1/2}^t$ is updated by the convective term as follows. If $\hat{j}_{i+1/2}^t$ or $v_{i+1/2}^t$ have positive direction,

$$\begin{aligned} (\text{conv})_{i+1/2}^t &= \frac{\hat{j}_{i+1/2}^t (v_{i+1/2}^t - v_{i-1/2}^t)}{\Delta x} \\ &\quad + \frac{v_{i+1/2}^t (\hat{j}_{i+1/2}^t - \hat{j}_{i-1/2}^t)}{\Delta x}. \end{aligned} \quad (\text{A8})$$

otherwise,

$$\begin{aligned} (\text{conv})_{i+1/2}^t &= \frac{\hat{j}_{i+1/2}^t (v_{i+3/2}^t - v_{i+1/2}^t)}{\Delta x} \\ &\quad + \frac{v_{i+1/2}^t (\hat{j}_{i+3/2}^t - \hat{j}_{i+1/2}^t)}{\Delta x}. \end{aligned} \quad (\text{A9})$$

Then $\hat{j}_{i+1/2}$ is updated by the convective terms, but with $\hat{j}_{i+1/2}$ and $v_{i+1/2}$ replaced by the values resulting from $\hat{j}_{i+1/2}$:

$$\frac{\hat{j}_{i+1/2}^{t+1} - \hat{j}_{i+1/2}^t}{\Delta t} = -(\text{conv})_{i+1/2}^t. \quad (\text{A10})$$

Finally, there is a need to define the boundary conditions for n and \hat{j} at the source and drain contacts, i.e., n_1 , n_N , $\hat{j}_{1/2}$, and $\hat{j}_{N+1/2}$. In the case of *ideal boundary conditions*, at the source terminal, we apply the Neumann boundary condition for the electron density, i.e., $n_1 = n_0$. At the drain terminal, we apply the Dirichlet boundary condition for the electron current, i.e., $\hat{j}_{N+1/2} = n_0 v_0$.

In the case of *nonideal boundary conditions*, the current at the source $\hat{j}_{1/2}$ and at the drain $\hat{j}_{N+1/2}$ are defined as

$$\hat{j}_{\frac{1}{2}} = \frac{C_S}{WC_{GC}} \frac{(n_1^t - n_1^{t-1})}{\Delta t}, \quad (\text{A11})$$

$$\hat{j}_{N+\frac{1}{2}} = -\frac{C_D}{WC_{GC}} \frac{(n_N^t - n_N^{t-1})}{\Delta t}, \quad (\text{A12})$$

which correspond to the discretized version of Eqs. (20) and (21) in the paper.

3. Discretization of the Maxwell's equations in the entire structure

We follow the methodology from [29] to discretize Maxwell's equations. For a transverse magnetic (TM) mode, the magnetic H and electric E fields can be written

Discretized Electron Transport Equation (1D)

$$n_i^{t+1} = n_i^t - \frac{\Delta t}{\Delta x} (j_{i+\frac{1}{2}}^t - j_{i-\frac{1}{2}}^t)$$

$$j_{i+\frac{1}{2}}^{t+1} = j_{i+\frac{1}{2}}^t - \Delta t \left[\frac{e}{m_e^*} n_{i+\frac{1}{2}}^t E_{i+\frac{1}{2}}^t - n \frac{\pi \hbar^2}{m_e^{*2}} \frac{\exp(\frac{E_F}{kT})}{\exp(\frac{E_F}{kT}) - 1} \frac{(n_{i+1}^t - n_i^t)}{\Delta x} - \frac{j_{i+\frac{1}{2}}^t}{\tau} - (conv)_{i+\frac{1}{2}}^t \right]$$

$$(conv)_{i+\frac{1}{2}}^t = \frac{j_{i+\frac{1}{2}}^t (v_{i+\frac{1}{2}}^t - v_{i-\frac{1}{2}}^t)}{\Delta x} + \frac{v_{i+\frac{1}{2}}^t (j_{i+\frac{1}{2}}^t - j_{i-\frac{1}{2}}^t)}{\Delta x}$$

Discretized Maxwell's Equation (2D)

$$H_z|_{i+\frac{1}{2},j+\frac{1}{2},k}^{t+\frac{1}{2}} = \left(\frac{1 - \frac{\sigma^* \Delta t}{2\mu_0 \mu_r}}{1 + \frac{\sigma^* \Delta t}{2\mu_0 \mu_r}} \right) H_z|_{i+\frac{1}{2},j+\frac{1}{2},k}^{t-\frac{1}{2}} + \left(\frac{\Delta t}{1 + \frac{\sigma^* \Delta t}{2\mu_0 \mu_r}} \right) \times \left[\left(\frac{E_x|_{i+\frac{1}{2},j+1,k}^t - E_x|_{i+\frac{1}{2},j,k}^t}{\Delta y} \right) - \left(\frac{E_y|_{i+1,j+\frac{1}{2},k}^t - E_y|_{i,j+\frac{1}{2},k}^t}{\Delta x} \right) \right]$$

$$E_x|_{i+\frac{1}{2},j,k}^{t+1} = \left(\frac{1 - \frac{\sigma \Delta t}{2\epsilon_0 \epsilon_r}}{1 + \frac{\sigma \Delta t}{2\epsilon_0 \epsilon_r}} \right) E_x|_{i+\frac{1}{2},j,k}^t + \left(\frac{\Delta t}{1 + \frac{\sigma \Delta t}{2\epsilon_0 \epsilon_r}} \right) \cdot \left[\left(\frac{H_z|_{i+\frac{1}{2},j+\frac{1}{2},k}^{t+\frac{1}{2}} - H_z|_{i+\frac{1}{2},j-\frac{1}{2},k}^{t+\frac{1}{2}}}{\Delta y} \right) - J_{x|_{i+\frac{1}{2},j,k}^{t+\frac{1}{2}}} \right]$$

$$E_y|_{i,j+\frac{1}{2},k}^{t+1} = \left(\frac{1 - \frac{\sigma \Delta t}{2\epsilon_0 \epsilon_r}}{1 + \frac{\sigma \Delta t}{2\epsilon_0 \epsilon_r}} \right) E_y|_{i,j+\frac{1}{2},k}^t + \left(\frac{\Delta t}{1 + \frac{\sigma \Delta t}{2\epsilon_0 \epsilon_r}} \right) \times \left[- \left(\frac{H_z|_{i+\frac{1}{2},j+\frac{1}{2},k}^{t+\frac{1}{2}} - H_z|_{i+\frac{1}{2},j-\frac{1}{2},k}^{t+\frac{1}{2}}}{\Delta x} \right) \right]$$

FIG. 8. Discretized system of equations.

in finite differences, respectively, as

$$E_x|_{i+1/2,j,k}^{t+1} = \left(\frac{1 - \sigma \Delta t / 2\epsilon_0 \epsilon_r}{1 + \sigma \Delta t / 2\epsilon_0 \epsilon_r} \right) E_x|_{i+1/2,j,k}^t + \left(\frac{\Delta t / \epsilon_0 \epsilon_r}{1 + \sigma \Delta t / 2\epsilon_0 \epsilon_r} \right) \cdot \left[\left(\frac{H_z|_{i+1/2,j+1/2,k}^{t+1/2} - H_z|_{i+1/2,j-1/2,k}^{t+1/2}}{\Delta y} \right) - \left(\frac{H_y|_{i+1/2,j,k+1/2}^{t+1/2} - H_y|_{i+1/2,j,k-1/2}^{t+1/2}}{\Delta z} \right) - J_x|_{i+1/2,j,k}^{t+1/2} \right], \quad (\text{A13})$$

$$H_z|_{i+1/2,j+1/2,k}^{t+1/2} = \left(\frac{1 - \sigma^* \Delta t / 2\mu_0 \mu_r}{1 + \sigma^* \Delta t / 2\mu_0 \mu_r} \right) H_z|_{i+1/2,j+1/2,k}^{t-1/2} + \left(\frac{\Delta t / \mu_0 \mu_r}{1 + \sigma^* \Delta t / 2\mu_0 \mu_r} \right) \cdot \left[\left(\frac{E_x|_{i+1/2,j+1,k}^t - E_x|_{i+1/2,j,k}^t}{\Delta y} \right) - \left(\frac{E_y|_{i+1,j+1/2,k}^t - E_y|_{i,j+1/2,k}^t}{\Delta x} \right) \right], \quad (\text{A14})$$

and H_x and H_y are zero. The linkage between the HDM equations and Maxwell's equations is given by the term J_x in Eq. (A13), where $J_x = ej/t_{\text{DEG}}$ (see Fig. 8).

Finally, in order to emulate an unbounded region, and thus estimate the fields radiated by the device under analysis in free space, an absorbing boundary condition (ABC) must be introduced at the outer lattice boundary to simulate the extension of the lattice to infinity. An approach to realize the ABC is to terminate the outer boundary of the space lattice in an absorbing material medium. Ideally, the absorbing medium is only a few lattice cells thick, reflectionless to all impinging waves over their full frequency spectrum, highly absorbing, and effective in the near field of a source or a scatterer. In the developed platform, this is accomplished with a PML, as first described by Berenger in [31].

- [1] Cisco, Cisco visual networking index: Global mobile data traffic forecast update, 2016–2021, White Paper (2017).
- [2] Ian F. Akyildiz, Josep M. Jornet, and Chong Han, Terahertz band: Next frontier for wireless communications, *Phys. Commun. (Elsevier) J.* **12**, 16 (2014).
- [3] Daniel M. Mittleman, Perspective: Terahertz science and technology, *J. Appl. Phys.* **122**, 230901 (2017).
- [4] Amir Nikpaik, Amir Hossein Masnadi Shirazi, Abdolreza Nabavi, Shahriar Mirabbasi, and Sudip Shekhar, A 219-to-231 GHz frequency-multiplier-based vco with 3% peak dc-to-rf efficiency in 65-nm cmos, *IEEE J. Solid-State Circuits* **53**, 389 (2018).

- [5] Hamidreza Aghasi, Andreia Cathelin, and Ehsan Afshari, A 0.92-THz sig power radiator based on a nonlinear theory for harmonic generation, *IEEE J. Solid-State Circuits* **52**, 406 (2017).
- [6] William R. Deal, Kevin Leong, Alexis Zamora, Ben Gorospe, Khanh Nguyen, and Xiao Bing Mei, in *Compound Semiconductor Integrated Circuit Symposium (CSICS), 2017 IEEE* (IEEE, Miami-Florida, 2017), p. 1.
- [7] Shu-Wei Huang, Jinghui Yang, Shang-Hua Yang, Mingbin Yu, Dim-Lee Kwong, Tanya Zelevinsky, Mona Jarrahi, and Chee Wei Wong, Globally stable microresonator tuning pattern formation for coherent high-power THz radiation on-chip, *Phys. Rev. X* **7**, 041002 (2017).
- [8] Tadao Nagatsuma, Guillaume Ducournau, and Cyril C. Renaud, Advances in terahertz communications accelerated by photonics, *Nat. Photonics* **10**, 371 (2016).
- [9] Quanyong Lu, Donghai Wu, Saumya Sengupta, Steven Slivken, and Manijeh Razeghi, Room temperature continuous wave, monolithic tunable THz sources based on highly efficient mid-infrared quantum cascade lasers, *Sci. Rep.* **6**, 23595 (2016).
- [10] Michael Dyakonov, and Michael Shur, Shallow water analogy for a ballistic field effect transistor: New mechanism of plasma wave generation by dc current, *Phys. Rev. Lett.* **71**, 2465 (1993).
- [11] W. Knap, J. Lusakowski, T. Parenty, S. Bollaert, A. Cappy, V. V. Popov, and M. S. Shur, Terahertz emission by plasma waves in 60 nm gate high electron mobility transistors, *Appl. Phys. Lett.* **84**, 2331 (2004).
- [12] S. Boubanga-Tombet, F. Teppe, D. Coquillat, S. Nadar, N. Dyakonova, H. Videlier, W. Knap, A. Shchepetov, C. Gardes, Y. Roelens, S. Bollaert, D. Seliuta, R. Vadoklis, and G. Valusis, Current driven resonant plasma wave detection of terahertz radiation: Toward the Dyakonov-Shur instability, *Appl. Phys. Lett.* **92**, 212101 (2008).
- [13] Abdelouahad El Fatimy, S. Boubanga Tombet, Frederic Teppe, Wojciech Knap, D. B. Veksler, S. Romyantsev, M. S. Shur, N. Pala, R. Gaska, and Q. Fareed, *et al.*, Terahertz detection by GaN/AlGaIn transistors, *Electron. Lett.* **42**, 1342 (2006).
- [14] S. Boubanga-Tombet, F. Teppe, J. Torres, A. El Moutaouakil, D. Coquillat, N. Dyakonova, C. Consejo, P. Arcade, P. Nouvel, and H. Marinchio, *et al.*, Room temperature coherent and voltage tunable terahertz emission from nanometer-sized field effect transistors, *Appl. Phys. Lett.* **97**, 262108 (2010).
- [15] T. Otsuji, T. Watanabe, S. A. Boubanga-Tombet, A. Satou, W. M. Knap, V. V. Popov, M. Ryzhii, and V. Ryzhii, Emission and detection of terahertz radiation using two-dimensional electrons in III-V semiconductors and graphene, *IEEE Trans. Terahertz Sci. Technol.* **3**, 63 (2013).
- [16] Frank J. Crowne, Contact boundary conditions and the Dyakonov-Shur instability in high electron mobility transistors, *J. Appl. Phys.* **82**, 1242 (1997).
- [17] Christian B. Mendl, and Andrew Lucas, Dyakonov-Shur instability across the ballistic-to-hydrodynamic cross over, *Appl. Phys. Lett.* **112**, 124101 (2018).
- [18] M. V. Cheremisin, and G. G. Samsonidze, Dyakonov-Shur instability in a ballistic field-effect transistor with a spatially nonuniform channel, *Semiconductors* **33**, 578 (1999).
- [19] Dmitry Svintsov, Exact solution for driven oscillations in plasmonic field-effect transistors, *Phys. Rev. Appl.* **10**, 024037 (2018).
- [20] Alexander L. Fetter, Electrodynamics of a layered electron gas. I. Single layer, *Ann. Phys.* **81**, 367 (1973).
- [21] Tsuneya Ando, Alan B. Fowler, and Frank Stern, Electronic properties of two-dimensional systems, *Rev. Mod. Phys.* **54**, 437 (1982).
- [22] Gregory R. Aizin, and Gregory C. Dyer, Transmission line theory of collective plasma excitations in periodic two-dimensional electron systems: Finite plasmonic crystals and Tamm states, *Phys. Rev. B* **86**, 235316 (2012).
- [23] If the inequality $kd \ll 1$ is not satisfied, an accurate description of the displacement currents in the contacts requires the use of the Shockley-Ramo theorem as it has been shown in [19] and Victor Ryzhii, Akira Satou, and Michael S Shur, Transit-time mechanism of plasma instability in high electron mobility transistors, *Phys. Status Solidi (A)* **202**, R113–R115 (2005).
- [24] A. P. Dmitriev, A. S. Furman, V. Yu Kachorovskii, G. G. Samsonidze, and Ge. G. Samsonidze, Numerical study of the current instability in a two-dimensional electron fluid, *Phys. Rev. B* **55**, 10319 (1997).
- [25] Kang Li, Yue Hao, Xiaoqi Jin, and Wu Lu, Hydrodynamic electronic fluid instability in gaas mesofets at terahertz frequencies, *J. Phys. D: Appl. Phys.* **51**, 035104 (2017).
- [26] Shubhendu Bhardwaj, Niru K. Nahar, Siddharth Rajan, and John L. Volakis, Numerical analysis of terahertz emissions from an ungated hemt using full-wave hydrodynamic model, *IEEE Trans. Electron Devices* **63**, 990 (2016).
- [27] Andreas Aste, and Rudiger Vahldieck, Time-domain simulation of the full hydrodynamic model, arXiv physics/0312021 (2003).
- [28] Atef Z. Elsherbeni, and Veysel Demir, *The Finite-Difference Time-Domain Method for Electromagnetics with MATLAB Simulations* (The Institution of Engineering and Technology, 2016).
- [29] Allen Taflove, and Susan C. Hagness, *Computational electrodynamics* (Artech House, 2005).
- [30] Jingwei Hu, and Li Wang, An asymptotic-preserving scheme for the semiconductor boltzmann equation toward the energy-transport limit, *J. Comput. Phys.* **281**, 806 (2015).
- [31] Jean-Pierre Berenger, A perfectly matched layer for the absorption of electromagnetic waves, *J. Comput. Phys.* **114**, 185 (1994).